PHYSICAL REVIEW C **102**, 054302 (2020)

Lifetime measurements in ^{44}Ti

K. Arnswald[1,*] P. Reiter,[1] A. Blazhev,[1] T. Braunroth,[1] A. Dewald,[1] M. Droste,[1] C. Fransen,[1] A. Goldkuhle,[1]
R. Hetzenegger,[1] R. Hirsch,[1] E. Hoemann,[1] L. Kaya,[1] L. Lewandowski,[1] C. Müller-Gatermann,[1,†] P. Petkov,[2,1]
D. Rosiak,[1] M. Seidlitz,[1] B. Siebeck,[1] A. Vogt,[1] D. Werner,[1] K. Wolf,[1] and K.-O. Zell[1]
[1] *Institut für Kernphysik, Universität zu Köln, 50937 Köln, Germany*
[2] *"Horia Hulubei" National Institute for Physics and Nuclear Engineering, R-76900 Bucharest-Măgurele, Romania*

(Received 24 July 2020; accepted 14 October 2020; published 2 November 2020)

Lifetimes of excited nuclear states were determined in ^{44}Ti using the recoil distance Doppler-shift technique and the Doppler-shift attenuation method. Results from the $K^{\pi} = 3^-$ band confirm isospin-symmetry breaking for the $3^-_1 \rightarrow 2^+_1$ $E1$ transition. The lifetime of the 4^-_1 state differs considerably from the previously known value. Good agreement is found for the 4^+_1 and 6^+_1 level lifetimes with respect to previous values. The experimental values are compared with large-scale shell-model calculations employing established interactions in the $0f1p$ shell, as well as a modern effective Hamiltonian including multiparticle multihole cross-shell configurations. Extended configuration spaces of this shell-model calculation allow for a detailed comparison with newly determined negative-parity states.

DOI: 10.1103/PhysRevC.102.054302

I. INTRODUCTION

The self-conjugated nucleus ^{44}Ti is a benchmark for present-day large-scale shell-model (LSSM) calculations in the full $0f1p$ shell northeast of the doubly magic nucleus ^{40}Ca. Several interactions such as the well-established FPD6 [1], KB3G [2], and GXPF1A [3] yield good agreement with various experimental observables, such as energy spectra or—with the inclusion of the Coulomb contributions—isospin-dependent effects like the mirror-energy differences (cf. Refs. [4–6]). However, for even-even nuclei these interactions are restricted to positive-parity states in the fp shell.

The latest calculations with the ZBM2M interaction [7] use the extended *hasp* model space [8] comprising the proton and neutron $1s_{1/2}$, $1d_{3/2}$, $0f_{7/2}$, $1p_{3/2}$ orbitals and surmount limitations of previous truncated schemes of the *sd* and fp main shells. They provide access to negative-parity states which—in the case of ^{44}Ti—cannot be calculated from the odd-parity fp orbitals. This interaction is based on the ZBM2 interaction [9] with adjustments of the $d_{3/2}$-$d_{3/2}$ monopole matrix elements. It demonstrated good agreement with experimental observations, i.e., excitation energies and charge radii, in ^{38}K and confirmed the relevance of cross-shell correlations in the vicinity of ^{40}Ca [7]. Moreover, results from the non-modified ZBM2 interaction reproduce well the experimentally observed energy spectra and reduced $E2$ strengths in stable Ca isotopes [9]. These results also include the even-even neighboring isotone ^{42}Ca and the $T_z = +2$ isobar ^{44}Ca of ^{44}Ti. However, the ZBM2M interaction was predominantly employed for calculations in the $Z \leqslant 20$ region [10–12]. Lifetime investigations in ^{44}Ti provide a fertile study ground for these calculations above the $Z = 20$ shell closure.

Recently, the first 2^+ level lifetimes in even-even $N = Z$ nuclei have been studied with an improved accuracy employing the Cologne coincidence-plunger setup [13]. The authors of this article report an increased $B(E2; 2^+_1 \rightarrow 0^+_{\text{g.s.}}) = 205^{+20}_{-17}\ e^2\,\text{fm}^4$ value in ^{44}Ti compared with previous measurements. Moreover, this result was not in agreement with values from shell-model interactions of the fp model space. This discrepancy was explained by multi-particle-hole (ph) cross-shell configurations in the vicinity of the $Z = 20$ shell closure.

The nuclear level lifetimes from higher-lying positive-parity states in ^{44}Ti are known from pioneering studies performed in the 1970s with limited precision [14–19]. Lifetimes of negative-parity states were studied by Kolata *et al.*, who determined a lifetime of $\tau = 3.9(13)$ ps for the 4^-_1 state [20]. From later lifetime and angular distribution measurements, performed by Dixon *et al.* [18], a lower lifetime limit of $\tau > 50$ ps was proposed for this state based on spin and parity arguments contradicting the lifetime value from Ref. [20]. The only evaluated lifetime exists for the negative-parity 3^-_1 bandhead [21] and it refers to a preliminary lifetime analysis from a conference proceeding in 2011 [22]. In this study a $B(E3; 3^-_1 \rightarrow 0^+_{\text{g.s.}}) \approx 3$ W.u. value is presented which corresponds to a lifetime of ≈31 ps including an adopted branching ratio of $I(3^-_1 \rightarrow 0^+_{\text{g.s.}})/I(3^-_1 \rightarrow 2^+_1) = 2.0(3)\%$ [21].

High-spin states in ^{44}Ti were investigated by O'Leary *et al.*, who observed rotational-like energy-level spacings between states placed upon the first-excited 0^+ state [23]. The energy levels were well reproduced by *df* shell-model calculations. These calculations use the positive-parity $d_{3/2}$ and negative-parity $f_{7/2}$ orbitals and allow for the derivation of the negative-parity band built upon the 3^-_1 state.

---

[*] konrad.arnswald@ikp.uni-koeln.de

[†] Present address: Physics Division, Argonne National Laboratory, 9700 South Cass Avenue, Lemont, Illinois 60439, USA.

2469-9985/2020/102(5)/054302(9)

On the theoretical side, ^{44}Ti is of importance for the investigation of α-cluster structures. These correlations are considerably distorted due to the strong effect of the spin-orbit force in the fp shell. Recent studies confirmed the applicability of the ^{40}Ca$+\alpha$ model (cf. Ref. [24]). Moreover, coexistence phenomena of the mean-field structure and α structures were investigated by the use of deformed-basis antisymmetrized molecular dynamics (AMD) exploiting the Gogny D1S force [25]. The authors verified the $\beta_2 = 0.25$ normally deformed $K^\pi = 3^-$ band with a dominant $1p1h$ intrinsic configuration. Detailed $B(E2)$ values from these approaches are available for positive-parity states [24,25].

The scarce and contradictory lifetime information of negative-parity states in ^{44}Ti together with recent theoretical advances of LSSM calculations motivates a refined study of lifetimes and reduced transition strengths in this nucleus. In this article, we report and discuss new results on lifetimes and reduced transition strengths in ^{44}Ti. This paper is organized as follows: the experimental setup is described in Sec. II, the data analysis and results are presented in Sec. III. A detailed comparison with results from shell-model calculations and systematics is reported in Sec. IV. The article closes with a summary and conclusions in Sec. V.

II. EXPERIMENTS

The lifetime experiments on ^{44}Ti were performed at the FN tandem accelerator at the Institute for Nuclear Physics, University of Cologne, Germany, using the setup of the Cologne coincidence plunger [26]. Excited states were populated by ^{40}Ca(^{6}Li, pn)^{44}Ti fusion-evaporation reactions at 20 MeV beam energy. The plunger target was made of 0.2 mg/cm^2 enriched ^{40}Ca evaporated on a 2 mg/cm^2 gold backing facing the beam. In addition, the target was sandwiched by a 0.1-mg/cm^2-thin gold layer which was evaporated onto the other side to reduce oxidation effects. Recoiling nuclei which left the target with a mean velocity of 0.81(5)% of the speed of light—which corresponds to $v = 2.43(15)$ μm/ps—were finally stopped in a 3.6-mg/cm^2-thick gold stopper. During the experiment, data were collected at seven target-to-stopper distances between 46 and 626 μm. Emitted γ rays were detected by twelve high-purity germanium (HPGe) detectors with relative efficiencies between 55% and 80% placed in three rings at polar angles of 0° (one detector), 45° (six detectors), and 142.3° (five detectors) with respect to the beam axis. Pileup and additional dead time were significantly reduced by 2-mm-thick sheets of lead and copper which were placed between target and end cap to shield the detectors from low-energy x-rays. In total, 10^{10} coincident γ-ray events were processed and recorded utilizing a synchronized 80-MHz XIA® Digital Gamma Finder (DGF) data-acquisition system and stored to disk. The data were sorted into γ-γ matrices employing the SOCO-V2 sort code [27] and analyzed utilizing the TV [28] software package.

Subsequently to the RDDS measurements, a DSAM run was performed employing a 0.2 mg/cm^2 enriched ^{40}Ca target which was centrally evaporated onto a 2 mg/cm^2 gold backing using a 2-mm aperture. To reduce oxidation effects of the target material, the ^{40}Ca layer was subsequently covered completely by a 0.5-mg/cm^2-thin gold fronting. The DSAM experiment was performed under similar experimental conditions with respect to the previous RDDS run. In total, 3.6×10^9 γ-γ events were recorded and stored to disk.

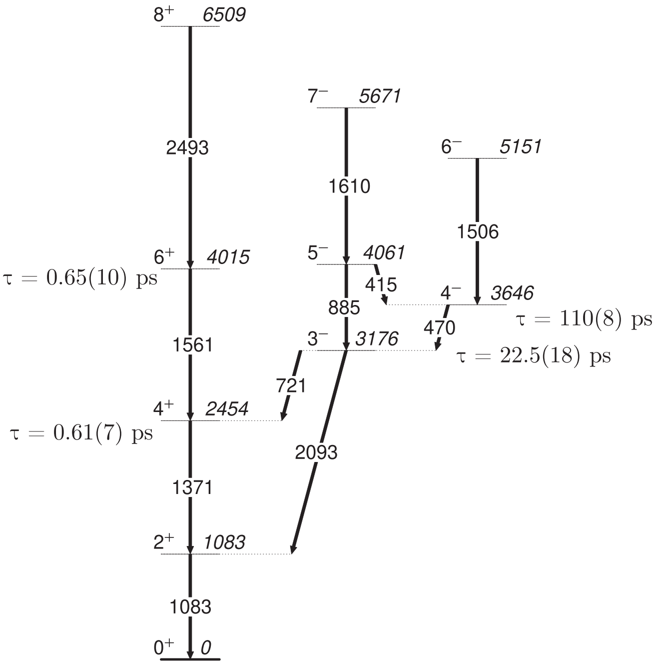

FIG. 1. Partial level scheme of ^{44}Ti. Dominant decay branches observed in both experiments as well as obtained level lifetimes are shown. All energies are given in keV.

III. DATA ANALYSIS AND RESULTS

The observed level scheme of populated excited states and measured lifetimes in ^{44}Ti is displayed in Fig. 1. The lifetime results, obtained in both experiments, are summarized in Table I.

A. Recoil distance Doppler shift

The lifetime analysis of the 3^-_1 and 4^-_1 states in ^{44}Ti is based on the recoil distance Doppler-shift (RDDS) technique and the differential decay-curve method (DDCM) [26,29]. The analysis was performed in the γ-γ coincidence mode using gates on completely shifted parts of directly feeding

TABLE I. Experimental lifetimes in ^{44}Ti from the present experiment are compared with previous experimental values. For each state the applied method and gating energies are summarized.

		Lifetime (ps)			E_γ (keV)	
E_x (keV)	J^π	Present	Literature	Method	Gate	Analyzed
1083	2^+		2.7(2) [13]			
2454	4^+	0.61(7)	0.60(11) [15]	DSAM	1561	1371
4015	6^+	0.65(10)	0.56(8) [18]	DSAM	2493	1561
3176	3^-	22.5(18)	≈31 [21,22]	RDDS	885	2093
3646	4^-	110(8)	3.9(13)[a] [20]	RDDS	1506	470

[a] Contradicts $\tau > 50$ ps as proposed in Ref. [18].

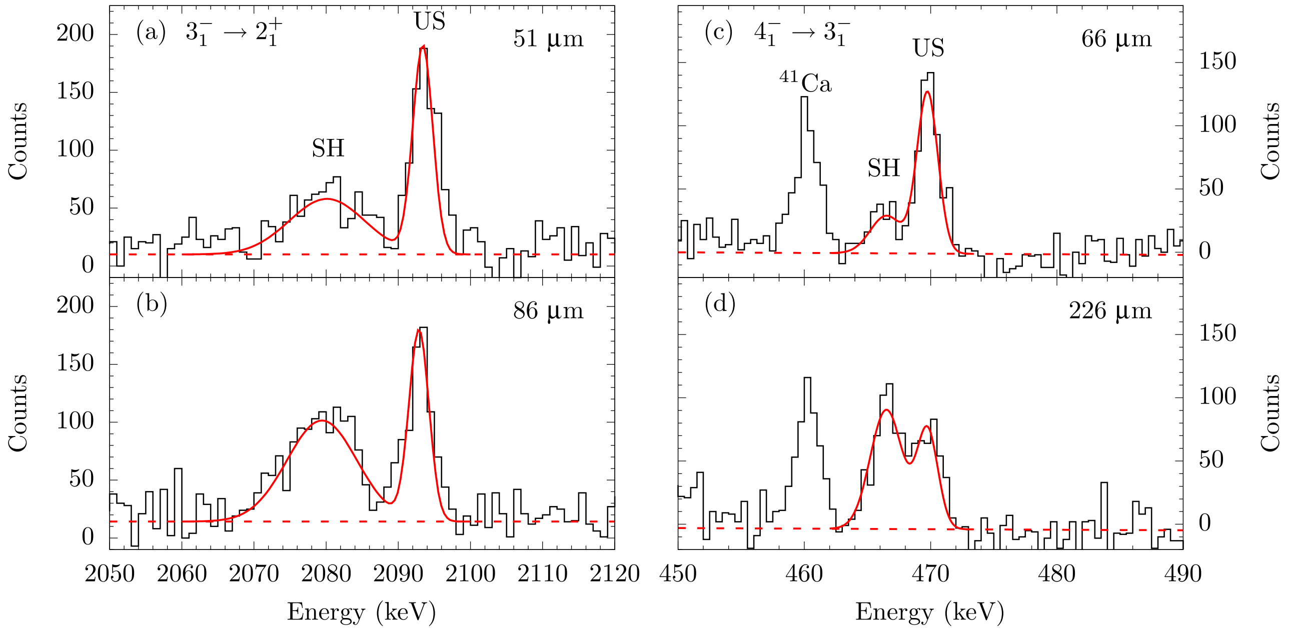

FIG. 2. Exemplary γ-ray energy spectra for the (a), (b) $3_1^- \to 2_1^+$ transition at 2093 keV and the (c), (d) $4_1^- \to 3_1^-$ transition at 470 keV for two different target-to-stopper distances. Spectra are produced by a gate on the shifted part of the direct feeders at 885 and 1506 keV, respectively. Unshifted (US) and shifted (SH) components as well as a contamination of ^{41}Ca to the $4_1^- \to 3_1^-$ transition are labeled. The Gaussian fits to the experimental spectra are given in a red solid lines, and the background is marked as dashed red (see text for details).

transitions from above. Lifetimes of the states of interest were subsequently determined from the peak volumes of shifted (SH) and unshifted (US) components of the depopulating transition. Exemplary gated γ-ray spectra are presented in Fig. 2 for the $3_1^- \to 2_1^+$ [Figs. 2(a) and 2(b)] and $4_1^- \to 3_1^-$ [Figs. 2(c) and 2(d)] transitions. Both spectra are shown for shorter target-to-stopper distances [Figs. 2(a) and 2(c)] and are compared with larger ones [Figs. 2(b) and 2(d)]. The peak volumes are determined via Gaussian fits. For consistency purposes, position and peak width of the unshifted component are assumed constant. Further details on RDDS analyses are contained in Ref. [26].

For each target-to-stopper distance x_i in the sensitive range, one lifetime τ_i is determined. The mean lifetime τ is determined from the weighted mean of all τ_i. γ-ray spectra from different detector-ring combinations are statistically independent and the final lifetime is determined from the weighted mean of the τ of each detector-ring combination. The statistical error is dominated by the variance of the single τ_i. The systematic uncertainties result from three main contributions. First, the error of the mean velocity. The mean velocity is deduced from the Doppler-shift of the 2093 keV transition at forward and backward angles. The uncertainty of the mean polar angle $\Delta\theta = 3^\circ$ results in a $\Delta\beta = 0.05\%$ systematic uncertainty of the velocity distribution. Second, the relative target-to-stopper distances were measured with a high precision of $\Delta x \leqslant 0.5\%$ relative to the absolute distances. Finally, contaminating transitions in general can have an impact on the experimental lifetime results but could be excluded by carefully selected narrow energy gates. The uncertainty of the final lifetime is deduced from the Gaussian error propagation.

The analysis of the 3_1^- and 4_1^- lifetimes is performed with the RDDS code NAPATAU [30]. In the case of the 3_1^- state, a gate was set on the shifted component of the direct-feeding $5_1^- \to 3_1^-$ transition at 885 keV. The lifetime is deduced from the unshifted and shifted intensities (I_{US} and I_{SH}) of the depopulating $3_1^- \to 2_1^+$ transition at 2093 keV displayed in Figs. 3(b) and 3(c). For the four distances in the sensitive range, lifetimes were obtained [see Fig. 3(a)] from second-order polynomial-fit functions to the experimental intensities of the Doppler-shifted components I_{SH}. The τ curve for the unshifted intensities is the derivative of this function with the proportionality constant $v \cdot \tau$. Both the fit function to I_{SH} as well as the τ curve for I_{US} are simultaneously χ^2 minimized to the experimental values. From both curves a lifetime τ_i is determined at each distance. The weighted mean lifetime from all distances in the sensitive range is determined from forward and backward angles for the 3_1^- state, yielding $\tau = 21.8(10)_{\mathrm{stat.}}(16)_{\mathrm{sys.}}$ ps and $\tau = 23.4(11)_{\mathrm{stat.}}(16)_{\mathrm{sys.}}$ ps, respectively. The weighted mean of both lifetimes amounts to $\tau(3_1^-) = 22.5(7)_{\mathrm{stat.}}(16)_{\mathrm{sys.}}$ ps.

Likewise, the lifetime of the 4_1^- state is determined via a gate on the shifted component of the direct-feeding $6_1^- \to 4_1^-$ transition at 1506 keV. Subsequently, unshifted and shifted intensities of the $4_1^- \to 3_1^-$ transition at 470 keV are analyzed [see Figs. 3(e) and 3(f)] for five distances in the sensitive range. The mean lifetime is obtained from the single τ_i in Fig. 3(d) and yields $\tau = 108(3)_{\mathrm{stat.}}(8)_{\mathrm{sys.}}$ ps and $\tau = 113(4)_{\mathrm{stat.}}(8)_{\mathrm{sys.}}$ ps from forward and backward angles, respectively. The weighted mean is $\tau(4_1^-) = 110(3)_{\mathrm{stat.}}(8)_{\mathrm{sys.}}$ ps. Exemplary τ curves of the 3_1^- and 4_1^- states are presented in Fig. 3.

B. Doppler-shift attenuation method

The Doppler-shift attenuation method (DSAM) was applied for the analysis of the short-lived 4_1^+ and 6_1^+ states. The

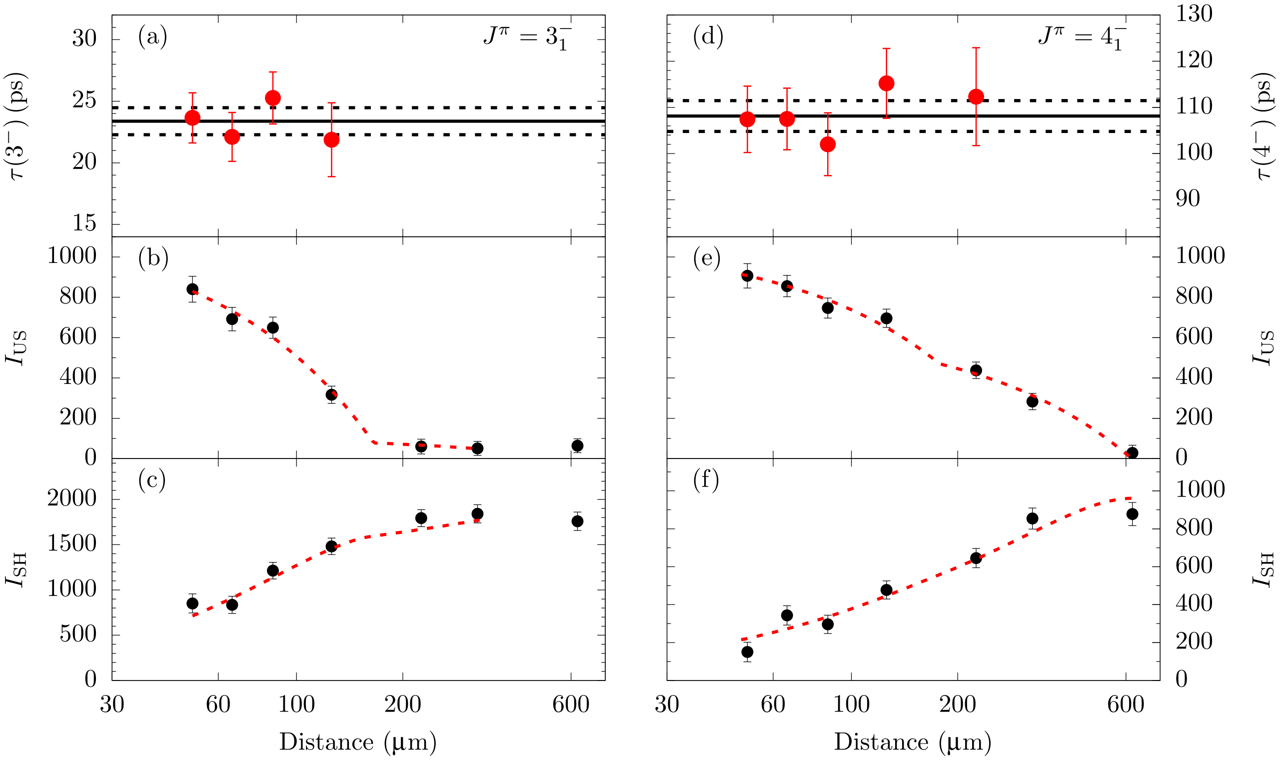

FIG. 3. Exemplary τ curves of the (a) 3_1^- state and (d) 4_1^- state at backward and forward angles, respectively. The weighted mean value is marked with a black solid line, the black dashed line indicates the statistical uncertainty. The respective (b), (e) unshifted and (c), (f) shifted intensities are presented with the corresponding polynomial-fit functions (dashed red curves). Lifetimes and γ-ray intensities are plotted against the offset-corrected relative target-to-stopper distances. Note the logarithmic distance scale.

slowing-down process of the nuclei of interest in the target and stopper material is described via Monte Carlo simulations performed by a modified version of the DESASTOP computer code [31,32]. The Monte Carlo simulations include the reaction kinematics, target and stopper properties, as well as the detector setup including finite opening angles. The electronic stopping powers for ^{44}Ti are obtained from Ref. [33]. For the contribution of the nuclear stopping, the LSS description [34] is considered as well as the parametrization of the universal scattering function for a Thomas-Fermi potential [35]. Microchanneling effects in the stopping medium are taken into account and are corrected for by a reduction factor of $f_n = 0.7$ (cf. Refs. [36–38] for further details).

In general, lifetime information can be obtained from the correlation of the slowing-down process of the recoiling nuclei of interest and the decay pattern of the studied nuclear states if both processes happen on the same timescales [39]. For the data analysis the differential decay-curve method was applied by using γ-γ gates on the directly feeding transition [40,41]. An energy gate onto any purely shifted part of the feeding transition generates a γ-ray spectrum of the depopulating transition which afterwards will be analyzed. The lineshape of this spectrum is a convolution of the Doppler-shifted energy spectrum (i.e., the energy spectrum projected on the recoil velocities corresponding to the energy gate) and the detector-response function. The lifetime analysis is based on a lineshape simulation which is compared with the experimental spectra. The simulation includes (i) the γ-ray energies of the unshifted feeding and depopulating transitions, (ii) the detector-response function, (iii) the time dependence of the velocity projections of the Doppler-shifted energies onto the observation angle of the detector setup, and (iv) the time-dependence of the population scheme of the level of interest. Further details on DSAM analyses are given in Refs. [40,41].

The lifetimes of the 4_1^+ and 6_1^+ states are analyzed by employing gates on the shifted component of the $6_1^+ \rightarrow 4_1^+$ and $8_1^+ \rightarrow 6_1^+$ feeding transitions, respectively. The resulting γ-ray spectra with the corresponding simulated lineshapes for the $4_1^+ \rightarrow 2_1^+$ and $6_1^+ \rightarrow 4_1^+$ transitions are presented in Figs. 4(a) and 4(b), respectively. Obviously, as both spectra show similar amounts of Doppler-shifted components with respect to the unshifted peak, the analyzed lifetimes cannot differ considerably. While the γ-γ statistics of the $4_1^+ \rightarrow 2_1^+$ transition amounts to 1500 counts in a single ring-ring combination, it diminishes to 400 counts for the elusive $6_1^+ \rightarrow 4_1^+$ transition. Nevertheless, the background level is reduced to <10 counts. Similar to the RDDS analysis, the generated γ-ray spectra are analyzed separately for forward and backward angles. The obtained lifetimes of the 6_1^+ state is determined from forward and backward angles, yielding $\tau = 0.64(12)$ ps and $\tau = 0.69(18)$ ps, respectively. The weighted mean of both values amounts to $\tau(6_1^+) = 0.65(10)$ ps. In the lifetime analysis of the 4_1^+ state this lifetime was included to the feeding scheme. The obtained lifetime of the 4_1^+ state is $\tau = 0.69(11)$ ps and $\tau = 0.56(9)$ ps for forward and backward angles,

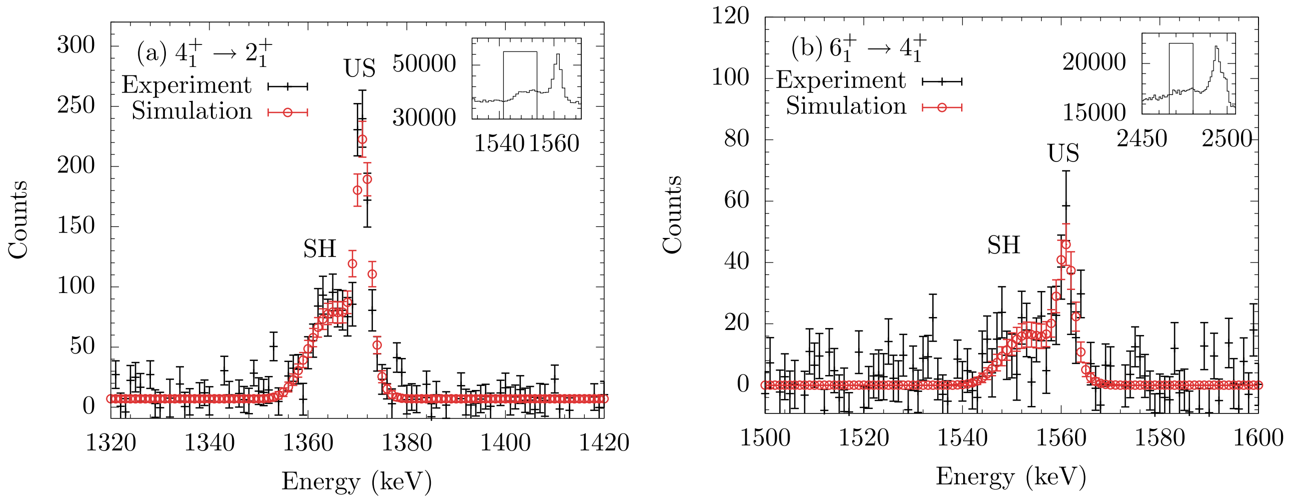

FIG. 4. γ-ray spectrum of the (a) $4_1^+ \to 2_1^+$ transition with a γ-energy gate on the purely shifted part of the $6_1^+ \to 4_1^+$ transition at 1541–1553 keV at backward angles. Similar data for the (b) $6_1^+ \to 4_1^+$ transition gated on the $8_1^+ \to 6_1^+$ transition at 2466–2480 keV. The γ-energy gates onto the direct feeding transitions are shown in the insets. The experimental data are shown as black crosses. The simulated lineshapes are given in open red circles.

respectively. The weighted mean yields $\tau(4_1^+) = 0.61(7)$ ps. The experimental uncertainties are dominated by the statistical errors which yield 90 and 40 fs for the 6_1^+ and 4_1^+ states, respectively. Systematic errors occur from the uncertainty of the slowing-down process, which is distributed over the uncertainties of the electronic and nuclear stopping powers and to the target width. These errors were conservatively estimated to not exceed 10% (cf. Ref. [41]) and are included in the final uncertainties.

IV. DISCUSSION

The measured lifetimes were converted to $B(\sigma\lambda)$ values and are compared with previous experimental data (see Table II). Furthermore, results for $B(\sigma\lambda)$ values from shell-model calculations were obtained and confronted with the new experimental findings. Comparisons are drawn along the ground-state band of ^{44}Ti up to the 12_1^+ state. The results are presented in Fig. 5.

The newly determined lifetimes of the 4_1^+ and 6_1^+ states correspond to $B(E2;\, 4_1^+ \to 2_1^+) = 276^{+36}_{-28}\ e^2\,\mathrm{fm}^4$ and $B(E2;\, 6_1^+ \to 4_1^+) = 135^{+25}_{-18}\ e^2\,\mathrm{fm}^4$, respectively. Both values are in a good agreement with previous measurements from the 1970s. The experimental uncertainty for the 4_1^+ lifetime was improved by 7%. The 3_1^- state decays via a 2093-keV $E1$ transition to the 2_1^+ state. The lifetime corresponds to $B(E1;3_1^- \to 2_1^+) = 3.0^{+0.3}_{-0.2} \times 10^{-6}\ e^2\,\mathrm{fm}^2$ and is in a fair agreement with the preliminary results from Ref. [22]. The

TABLE II. Experimental reduced transition strengths of ^{44}Ti from the present experiment are compared with previous experimental values. The results on reduced transition strengths and excitation energies from Ref. [21] are compared with four different shell-model calculations with $e_\pi = 1.5e$, $e_\nu = 0.5e$. See text for details.

	E_i (keV)					$B(\sigma\lambda)$ (W.u.)					
	Experiment	Theory				Experiment		Theory			
$J_i^\pi \xrightarrow{\sigma\lambda} J_f^\pi$	Literature	GXPF1A	KB3G	FPD6	ZBM2M	Present	Previous	GXPF1A	KB3G	FPD6	ZBM2M
$2_1^+ \xrightarrow{E2} 0_{\mathrm{g.s.}}^+$	1083	1287	1300	1300	1096		$22.0^{+1.8}_{-1.5}$ [13]	11.4	12.9	15.2	24.5
$4_1^+ \xrightarrow{E2} 2_1^+$	2454	2381	2430	2498	2696	30^{+4}_{-3}	30^{+7}_{-5} [15]	14.8	17.0	20.6	35.4
$6_1^+ \xrightarrow{E2} 4_1^+$	4015	3113	3317	3776	4511	15^{+3}_{-2}	17^{+3}_{-2} [18]	11.6	14.2	17.4	22.5
$8_1^+ \xrightarrow{E2} 6_1^+$	6509	5210	5589	6248	6081		>1.3[a][17]	7.8	10.1	12.1	23.2
$10_1^+ \xrightarrow{E2} 8_1^+$	7671	6368	6868	7614	7292		16^{+4}_{-2}[a] [17]	10.0	11.3	11.8	3.7
$12_1^+ \xrightarrow{E2} 10_1^+$	8040	6776	7484	8312	7723		$4.4^{+1.1}_{-0.7}$ [19]	5.9	6.6	6.8	4.1
$3_1^- \xrightarrow{E1} 2_1^+$	3176				3544	$3.7(3) \times 10^{-6}$	$\approx 2.7 \times 10^{-6}$ [22]				0
$4_1^- \xrightarrow{E2} 3_1^-$[b]	3646				2844	32^{+3}_{-2}	1000^{+500}_{-200} [20]				0.3
$4_1^- \xrightarrow{M1} 3_1^-$ [b]						$1.4^{+0.7}_{-0.4} \times 10^{-4}$	$4^{+3}_{-2} \times 10^{-3}$ [20]				1.7×10^{-6}

[a] $B(E2)$ value assumes 100% branching.

[b] With $|\delta| = 4.2(8)$ [42].

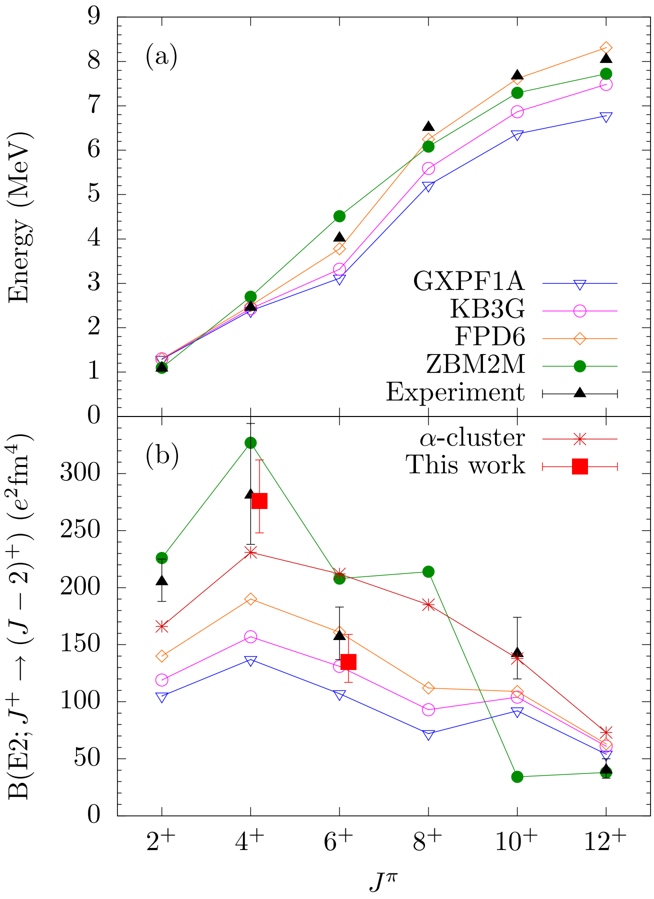

FIG. 5. (a) Experimental and theoretical excitation energies and (b) $B(E2)$ values of the ground-state band in ^{44}Ti. $B(E2)$ values from this work are given by red squares. Previously adopted experimental transition strengths (black filled triangles) are taken from the corresponding lifetimes given in Refs. [13,15,17–19]. Shell-model calculations employing the GXPF1A (blue open triangles), KB3G (purple open circles), FPD6 (orange open diamonds), and ZBM2M (green filled circles) interactions are shown. $B(E2)$ values are compared with results from an α-cluster model (dark red stars) taken from Ref. [24].

4_1^- state is depopulated via a mixed $E2$-$M1$ transition. The lifetime converts into $B(E2; 4_1^- \to 3_1^-) = 290(20)\ e^2\ \mathrm{fm}^4$ and $B(M1; 4_1^- \to 3_1^-) = 2.6^{+1.3}_{-0.7} \times 10^{-4}\ \mu_N^2$. The applied mixing ratio is given in Ref. [42] and yields $\delta = 4.2(8)$. The obtained result differs considerably from the value given in Ref. [20]. However, a larger lifetime was already indicated by Dixon *et al.* [18] and fits the present observations.

For the theoretical description of the excitation energies and the $B(E2)$ values of the ground-state band, shell-model calculations were performed employing the K-SHELL code [43,44] as well as the code NUSHELLX@MSU [45]. The fp model space comprises the $0f_{7/2}$, $1p_{3/2}$, $1p_{1/2}$, and $0f_{5/2}$ orbitals coupled to a ^{40}Ca core. Three interactions were employed for comparison with the present experimental data: FPD6 [1], KB3G [2], and GXPF1A [3]. Moreover, the ZBM2M shell-model interaction [7] was employed for the calculation of negative-parity states and to investigate the impact of cross-shell correlations in ^{44}Ti. This interaction uses the extended *hasp* model space comprising the proton and neutron $1s_{1/2}$, $1d_{3/2}$, $0f_{7/2}$, $1p_{3/2}$ orbitals coupled to a ^{28}Si core. For nuclei in the region of the *sd* and fp shells, reduced proton charges of $e_\pi = 1.15e$ to $1.31e$ provided reasonable results along $N = Z$ [46,47]. However, standard effective charges $e_\pi = 1.5e$ and $e_\nu = 0.5e$ are used for all shell-model calculations in order to approach the impact of core excitations in ^{44}Ti. For the derivation of $B(M1)$ strengths, effective spin g-factors with $g^s_{\mathrm{effective}} = 0.7 g^s_{\mathrm{free}}$ (i.e., $g^s_\pi = 3.91$ and $g^s_\nu = -2.678$) were used, which is justified because the spin-orbit partners are not present in the model space. Furthermore, these values exactly reproduce the experimental g-factors of the 2_1^+ reference state [48]. The shell-model results are summarized in Table II and displayed in Fig. 5.

As observed in Fig. 5(a), the four shell-model interactions reproduce the trend of the excitation energies of the ground-state band in ^{44}Ti quite well. Nevertheless, there are some deviations which have significant impact on the evolution of the $B(E2)$ values discussed hereinafter. The excitation energy of the 2_1^+ state is in very good agreement with the result from the ZBM2M interaction but is overestimated by the other three interactions by approximately 200 keV. The 4_1^+ state excitation energy is well reproduced by the three fp shell interactions and is overestimated by the ZBM2M interaction by ≈250 keV. The energy of the 6_1^+ state is still overestimated by the ZBM2M interaction while being underpredicted by the other three interactions. Thenceforward, the ZBM2M, GXPF1A, and KB3G interactions underestimate the evolution of the 8_1^+, 10_1^+, and 12_1^+ excitation energy, whereas the FPD6 interaction is in fair agreement with the experimental observations. In addition, the ZBM2M interaction opens the possibility to calculate excitation energies from negative-parity states. The energy of the 3_1^- state yields 3544 keV compared with the experimental value of 3176 keV. However, the excitation energy of the 4_1^- state is not reproduced (2844 keV compared with 3646 keV), moving the 4_1^- state below the 3_1^- bandhead.

The derived $B(E2)$ values exhibit a very different evolution along the yrast band for the GXPF1A, KB3G, and FPD6 interactions on the one hand and the ZBM2M interaction on the other hand [see Fig. 5(b)]. The three fp-shell interactions show a very similar evolution along the ground-state band. As already discussed in Ref. [13], the theoretical description of the first-excited 2^+ state underestimates the experimental result. This behavior continues for the 4_1^+ state. The theoretical results match the experimental results first for the $6_1^+ \to 4_1^+$ transition where the $B(E2)$ nearly halves. Thenceforward, all three interactions are in good agreement with the experimental observations. The ^{40}Ca core excitations have predominantly low-spin configurations which, therefore, influence most the wave functions of the low-spin states. Even by the use of standard effective charges, the fp shell interactions do not match the experimental values. For the $2_1^+ \to 0^+_{\mathrm{g.s.}}$ and $4_1^+ \to 2_1^+$ transitions only the new ZBM2M interaction with the extended *hasp* model space provides a good description. This is due to the account of particle-hole excitations for the low-spin states. Their amount is deduced from the wave functions and it yields more than 88% of core-excited configurations for the states up to 6_1^+. The higher-lying states are predominantly of

$f_{7/2}$ character manifested by a general decrease in collectivity. This is differently modeled by the ZBM2M calculation. Clear deviations between the different theoretical approaches are observed for the 8_1^+ and 10_1^+ states. The ZBM2M interaction overestimates the values of the other interactions for the 8_1^+ state, whereas experimental and theoretical values for the 10_1^+ state are considerably underestimated. The 12_1^+ isomer is in good agreement with the shell-model result. The ZBM2M interaction is competitive for the description of low-spin yrast states in ^{44}Ti although its predictive power decreases with higher spins.

The experimental $B(E2)$ values from the ground-state band are furthermore compared with theoretical values from the α-cluster model reported by Ohkubo *et al.* [24]. The group uses an α-like excitation of a ^{40}Ca core employing density-dependent M3Y (DDM3Y) double folding potentials without any effective charges. $B(E2)$ values extracted from this model are displayed in Fig. 5(b). They show a trend similar to the ZBM2M values although they evolve smoother along the ground-state band. This model reproduces the enhanced collectivity for the 2_1^+ and 4_1^+ states well and is in perfect agreement with the $B(E2)$ value of the 10_1^+ state. Similar to the ZBM2M calculation, the $B(E2)$ value from the 6_1^+ state is overestimated by the α-cluster model. Overall, the evolution of the ground-state band transition strengths are reproduced quite well by this model. This also supports the argument of the importance of an excited ^{40}Ca core for an adequate description of transition strengths from low-energy states in ^{44}Ti.

Transition strengths from negative-parity states were calculated with the ZBM2M interaction. However, the calculated $B(E1; 3_1^- \rightarrow 2_1^+)$ value is equal to zero. At first glance, the shell model supports the exceptionally low $B(E1) = 3.7(3) \times 10^{-6}$ W.u. value. The finite experimental value can be explained by isospin-symmetry breaking as both states—the 3_1^- and 2_1^+—are calculated to have isospin $T = 0$. Due to the isovector character of the $E1$ transition operator, the shell model yields $B(E1) = 0$. This slow $E1$ transition in ^{44}Ti exhibits a drop in collectivity with respect to the isotopic and isotonic neighbors ^{46}Ti and ^{42}Ca of two to three orders of magnitude. Even for the $T_z = +2$ isospin partner ^{44}Ca the $B(E1; 3_1^- \rightarrow 2_1^+)$ value amounts to $2.5(12) \times 10^{-4}$ W.u. [21]. The calculated $M1$ and $E2$ reduced transition strengths of the $4_1^- \rightarrow 3_1^-$ transition underpredict the experimental values by two orders of magnitude (see Table II). The shell-model calculations support a dominating $E2$ character of the $4_1^- \rightarrow 3_1^-$ transition. The interaction yields a multipole-mixing ratio of 6.3 and is comparable with the experimentally determined $|\delta| = 4.2(8)$ [42].

To give a more detailed interpretation of the lifetime of the 4_1^- state, the decomposition of the total wave function configuration into its proton and neutron components was calculated for selected states with the ZBM2M interaction. The decomposition matrix is symmetric due to the self-conjugated nature of ^{44}Ti. The 4_1^- state can be predominantly decomposed into $4^- \otimes 0^+$ (22%), $4^- \otimes 2^+$ (28%), and $5^- \otimes 2^+$ (15%) coupled proton or neutron configurations. While the 0^+ and 2^+ configurations are of $2p2h$ (24%) and $4p4h$ (16%) character, the configurations coupled to 4^- and 5^- are predominantly of $3p3h$ character: $d_{3/2}^{-1} s_{1/2}^{-2} f_{7/2}^{5}$ (30%), $d_{3/2}^{-2} s_{1/2}^{-1} f_{7/2}^{5}$ (9%), and $d_{3/2}^{-1} s_{1/2}^{-2} p_{3/2}^{1} f_{7/2}^{4}$ (5%). Major components of the 3_1^- state originate from $3^- \otimes 0^+$ (31%), $2^- \otimes 2^+$ (22%), and $5^- \otimes 2^+$ (13%) nucleon couplings. Similar to the 4^- state, the positive-parity configurations are $2p2h$ (23%) and $4p4h$ (4%) excitations plus an additional amount of $0p0h$ (12%) configurations. In contrast with the 4_1^- state, the negative-parity configurations of the 3_1^- are dominated by $1p1h$ (28%) (19% $s_{1/2}^{-1} f_{7/2}^{3}$ and 9% $d_{3/2}^{-1} f_{7/2}^{3}$) nucleon configurations. The $3p3h$ configurations $d_{3/2}^{-2} s_{1/2}^{-1} f_{7/2}^{5}$ (12%) and $d_{3/2}^{-1} s_{1/2}^{-2} f_{7/2}^{5}$ (2%) are calculated to an amount of 14%.

As the $E2$ and $M1$ one-body transition operators in the shell-model calculation can only connect configurations differing by maximum $1p1h$ excitation, the transition $4_1^- \rightarrow 3_1^-$ is limited to $3p3h$ configurations and is predominantly of $d_{3/2} \leftrightarrow s_{1/2}$ character. This explains the small transition strength calculated by the ZBM2M interaction, especially as the spin-orbit partners are not available in the given model space, the $B(M1)$ strength is hindered. Therefore, calculations in the full $sdpf$ model space are needed for a refined theoretical description of the $4_1^- \rightarrow 3_1^-$ transition.

V. CONCLUSIONS

In summary, lifetimes of negative and positive-parity states in the $N = Z$ nucleus ^{44}Ti were measured with the RDDS technique and the DSA method. The present results for the 4_1^+ and 6_1^+ states yield good agreement with previous measurements. Deviations were found for the 3_1^- and 4_1^- states. In the case of the 3_1^- state, only preliminary values are available in the literature. The higher lifetime of the 4_1^- state has been predicted by Dixon *et al.* [18]. The comparison with shell-model calculations yield ambiguous conclusions. The ZBM2M interaction reproduces the 2_1^+ and 4_1^+ transition probabilities well but falls short for higher spins. The GXPF1A, KB3G, and FPD6 interaction are in good agreement with the $B(E2; 6_1^+ \rightarrow 4_1^+)$ value and reproduce the trend up to the 12^+ isomer. $B(E2)$ values from the ground-state band were well reproduced by results from the $\alpha + {}^{40}\mathrm{Ca}(I^\pi)$ model reported in Ref. [24]. Reduced transition strengths from the negative-parity band in ^{44}Ti were compared with shell-model results for the first time. The finite experimental value of $B(E1; 3_1^- \rightarrow 2_1^+) = 3.7(3) \times 10^{-6}$ W.u. indicates isospin-symmetry breaking and remains challenging to be reproduced within the shell model. The derived transition strengths of the $4_1^- \rightarrow 3_1^-$ transition show the same trend to a higher lifetime but even underestimate the present $B(\sigma\lambda)$ values. For the 8_1^+ state only an upper lifetime limit of $\tau < 0.7$ ps is available in literature. Precise lifetime measurements of this state can close the gap within the yrast band towards the 12^+ isomer and will help to solve the puzzle of the different shell-model descriptions. On the theory side, full $sdpf$ shell-model calculations are needed to properly discuss the $B(M1)$ strength of the $4_1^- \rightarrow 3_1^-$ transition.

ACKNOWLEDGMENTS

We acknowledge fruitful discussions with N. Shimizu. We thank the IKP FN Tandem accelerator team for the professional support during the experiment.

[1] W. A. Richter, M. G. Van Der Merwe, R. E. Julies, and B. A. Brown, New effective interactions for the $0f1p$ shell, Nucl. Phys. A **523**, 325 (1991).

[2] A. Poves, J. Sánchez-Solano, E. Caurier, and F. Nowacki, Shell model study of the isobaric chains $A = 50$, $A = 51$ and $A = 52$, Nucl. Phys. A **694**, 157 (2001).

[3] M. Honma, T. Otsuka, B. A. Brown, and T. Mizusaki, Shell-model description of neutron-rich pf-shell nuclei with a new effective interaction GXPF1, Eur. Phys. J. A **25**, 499 (2005).

[4] S. M. Lenzi and M. A. Bentley, Test of Isospin Symmetry-isospin symmetry Along the $N = Z$ Line, in *The Euroschool Lectures on Physics with Exotic Beams, Vol. III*, edited by J. S. Al-Khalili and E. Roeckl (Springer, Berlin, Heidelberg, 2009), Vol. 764, pp. 57–98.

[5] F. Brandolini, S. M. Lenzi, D. R. Napoli, R. V. Ribas, H. Somacal, C. A. Ur, D. Bazzacco, J. A. Cameron, G. de Angelis, M. De Poli, C. Fahlander, A. Gadea, S. Lunardi, G. Martínez-Pinedo, N. H. Medina, C. Rossi Alvarez, J. Sánchez-Solano, and C. E. Svensson, Precise DSAM lifetime measurements in ^{48}Cr and ^{50}Cr as a test of large scale shell model calculations, Nucl. Phys. A **642**, 387 (1998).

[6] M. A. Bentley, S. J. Williams, D. T. Joss, C. D. O'Leary, A. M. Bruce, J. A. Cameron, M. P. Carpenter, P. Fallon, L. Frankland, W. Gelletly, C. J. Lister, G. Martínez-Pinedo, A. Poves, P. H. Regan, P. Reiter, B. Rubio, J. Sanchez Solano, D. Seweryniak, C. E. Svensson, S. M. Vincent, and D. D. Warner, Mirror symmetry at high spin in ^{51}Fe and ^{51}Mn, Phys. Rev. C **62**, 051303(R) (2000).

[7] M. L. Bissell, J. Papuga, H. Naïdja, K. Kreim, K. Blaum, M. De Rydt, R. F. Garcia Ruiz, H. Heylen, M. Kowalska, R. Neugart, G. Neyens, W. Nörtershäuser, F. Nowacki, M. M. Rajabali, R. Sanchez, K. Sieja, and D. T. Yordanov, Proton-Neutron Pairing Correlations in the Self-Conjugate Nucleus ^{38}K Probed via a Direct Measurement of the Isomer Shift, Phys. Rev. Lett. **113**, 052502 (2014).

[8] H. Hasper, Large scale shell-model calculations in the upper part of the *sd* shell: General description and energy levels for $A = 36$–39, Phys. Rev. C **19**, 1482 (1979).

[9] E. Caurier, K. Langanke, G. Martínez-Pinedo, F. Nowacki, and P. Vogel, Shell model description of isotope shifts in calcium, Phys. Lett. B **522**, 240 (2001).

[10] R. F. Garcia Ruiz, M. L. Bissell, K. Blaum, A. Ekström, N. Frömmgen, G. Hagen, M. Hammen, K. Hebeler, J. D. Holt, G. R. Jansen, M. Kowalska, K. Kreim, W. Nazarewicz, R. Neugart, G. Neyens, W. Nörtershäuser, T. Papenbrock, J. Papuga, A. Schwenk, J. Simonis, K. A. Wendt, and D. T. Yordanov, Unexpectedly large charge radii of neutron-rich calcium isotopes, Nat. Phys. **12**, 594 (2016).

[11] D. M. Rossi, K. Minamisono, H. B. Asberry, G. Bollen, B. A. Brown, K. Cooper, B. Isherwood, P. F. Mantica, A. Miller, D. J. Morrissey, R. Ringle, J. A. Rodriguez, C. A. Ryder, A. Smith, R. Strum, and C. Sumithrarachchi, Charge radii of neutron-deficient ^{36}K and ^{37}K, Phys. Rev. C **92**, 014305 (2015).

[12] J. Kostensalo, J. Suhonen, and K. Zuber, Shell-model computed cross sections for charged-current scattering of astrophysical neutrinos off ^{40}Ar, Phys. Rev. C **97**, 034309 (2018).

[13] K. Arnswald, T. Braunroth, M. Seidlitz, L. Coraggio, P. Reiter, B. Birkenbach, A. Blazhev, A. Dewald, C. Fransen, B. Fu, A. Gargano, H. Hess, R. Hirsch, N. Itaco, S. M. Lenzi, L. Lewandowski, J. Litzinger, C. Müller-Gatermann, M. Queiser, D. Rosiak, D. Schneiders, B. Siebeck, T. Steinbach, A. Vogt, K. Wolf, and K. O. Zell, Enhanced collectivity along the $N = Z$ line: Lifetime measurements in ^{44}Ti, ^{48}Cr, and ^{52}Fe, Phys. Lett. B **772**, 599 (2017).

[14] R. B. Huber, W. Kutschera, C. Signorini, and P. Blasi, Gamma transitions in ^{44}Ti and ^{48}Cr from heavy ion induced reactions, J. Phys. Colloques **32**, C6–207 (1971).

[15] W. R. Dixon, R. S. Storey, and J. J. Simpson, Lifetimes of ^{44}Ti levels, Nucl. Phys. A **202**, 579 (1973).

[16] J. J. Simpson, W. R. Dixon, and R. S. Storey, Evidence for Rotational Bands in ^{44}Ti, Phys. Rev. Lett. **31**, 946 (1973).

[17] J. J. Simpson, W. Dünnweber, J. P. Wurm, P. W. Green, J. A. Kuehner, W. R. Dixon, and R. S. Storey, Yrast levels in ^{44}Ti, Phys. Rev. C **12**, 468 (1975).

[18] W. R. Dixon, R. S. Storey, and J. J. Simpson, Levels of ^{44}Ti from the ^{40}Ca$(\alpha,\gamma)^{44}$Ti reaction, Phys. Rev. C **15**, 1896 (1977).

[19] J. Britz, A. Chevallier, J. Chevallier, and B. Haas, Lifetime of the 8040 keV state in ^{44}Ti, Nucl. Phys. A **262**, 189 (1976).

[20] J. J. Kolata, J. W. Olness, and E. K. Warburton, High-spin states in ^{44}Ti and ^{44}Sc, Phys. Rev. C **10**, 1663 (1974).

[21] Evaluated Nuclear Structure Data File (ENSDF), (2020), http://www.nndc.bnl.gov/ensdf.

[22] C. Michelagnoli, C. A. Ur, E. Farnea, S. M. Lenzi, S. Lunardi, F. Recchia, N. Marginean, D. Bucurescu, G. Cata-Danil, D. Delenau, D. Filipescu, D. Ghita, T. Glodariu, R. Marginean, C. Mihai, A. Negret, S. Pascu, T. Sava, L. Stroe, and G. Suliman, Lifetime measurement in $N = Z$ nucleus ^{44}Ti, Acta Phys. Pol., B **42**, 825 (2011).

[23] C. D. O'Leary, M. A. Bentley, B. A. Brown, D. E. Appelbe, R. A. Bark, D. M. Cullen, S. Ertürk, A. Maj, and A. C. Merchant, Nonyrast high-spin states in $N = Z$ ^{44}Ti, Phys. Rev. C **61**, 064314 (2000).

[24] S. Ohkubo, Y. Hirabayashi, and T. Sakuda, α-cluster structure of ^{44}Ti in core-excited $\alpha + {}^{40}$Ca model, Phys. Rev. C **57**, 2760 (1998).

[25] M. Kimura and H. Horiuchi, Coexistence of cluster structure and superdeformation in ^{44} Ti, Nucl. Phys. A **767**, 58 (2006).

[26] A. Dewald, O. Möller, and P. Petkov, Developing the recoil distance Doppler-shift technique towards a versatile tool for lifetime measurements of excited nuclear states, Prog. Part. Nucl. Phys. **67**, 786 (2012).

[27] N. Saed-Samii, Ph.D. thesis, Universität zu Köln, 2013 (unpublished).

[28] J. Theuerkauf, S. Esser, S. Krink, M. Luig, N. Nicolay, O. Stuch, and H. Wolters, Program TV, Institute for Nuclear Physics, Cologne, Germany.

[29] A. Dewald, S. Harissopulos, and P. von Brentano, The differential plunger and the differential decay curve method for the analysis of recoil distance Doppler-shift data, Z. Phys. A **334**, 163 (1989).

[30] B. Saha, Bestimmung der Lebensdauern kollektiver Kernanregungen in 124-Xe und Entwicklung von entsprechender Analysesoftware, Ph.D. thesis, Universität zu Köln, 2004, https://kups.ub.uni-koeln.de/1246/.

[31] G. Winter, The application of lineshape analysis in plunger measurements, Nucl. Instrum. Methods Phys. Res. **214**, 537 (1983).

[32] G. Winter, ZfK Rossendorf Report ZfK-497 (1983).

[33] L. C. Northcliffe and R. F. Schilling, Range and stopping-power tables for heavy ions, At. Data Nucl. Data Tables **7**, 233 (1970).

[34] J. Lindhard, M. Scharff, and H. E. Schiøtt, Kgl. Dan. Vid. Selsk. Mat. Fys. Medd. **33**, 14 (1963).

[35] W. M. Currie, A Monte Carlo programme for Doppler shift analysis, Nucl. Instrum. Methods **73**, 173 (1969).

[36] J. Keinonen, Use of capture reactions to measure short lifetimes by the DSA method, AIP Conf. Proc. **125**, 557 (1985).

[37] J. F. Ziegler and J. P. Biersack, The Stopping and Range of Ions in Matter, in *Treatise on Heavy-Ion Science: Volume 6: Astrophysics, Chemistry, and Condensed Matter*, edited by D. A. Bromley (Springer US, Boston,1985), pp. 93–129.

[38] J. Keinonen, Reliability of short lifetimes measured by the Doppler shift attenuation method, AIP Conf. Proc. **238**, 383 (1991).

[39] T. K. Alexander and J. S. Forster, Lifetime Measurements of Excited Nuclear Levels by Doppler-Shift Methods, in *Advances in Nuclear Physics: Volume 10*, edited by M. Baranger and E. Vogt (Springer US, Boston,1978), pp. 197–331.

[40] P. Petkov, D. Tonev, J. Gableske, A. Dewald, and P. von Brentano, Lifetime analysis using the Doppler-shift attenuation method with a gate on feeding transition, Nucl. Instrum. Methods Phys. Res., Sect. A **437**, 274 (1999).

[41] P. Petkov, C. Müller-Gatermann, D. Werner, A. Dewald, A. Blazhev, C. Fransen, J. Jolie, S. Ohkubo, and K. O. Zell, New lifetime measurements for the lowest quadrupole states in ^{20,22}Ne and possible explanations of the high collectivity of the depopulating $E2$ transitions, Phys. Rev. C **100**, 024312 (2019).

[42] W. R. Dixon, R. S. Storey, and J. J. Simpson, Spins of the 3176 and 3646 keV levels of ^{44}Ti, Nucl. Phys. A **363**, 173 (1981).

[43] Noritaka Shimizu, Nuclear shell-model code for massive parallel computation, KSHELL, arXiv:1310.5431.

[44] N. Shimizu, T. Mizusaki, Y. Utsuno, and Y. Tsunoda, Thick-restart block Lanczos method for large-scale shell-model calculations, Comput. Phys. Commun. **244**, 372 (2019).

[45] B. A. Brown and W. D. M. Rae, The shell-model code NuShellX@MSU, Nucl. Data Sheets **120**, 115 (2014).

[46] R. du Rietz, J. Ekman, D. Rudolph, C. Fahlander, A. Dewald, O. Möller, B. Saha, M. Axiotis, M. A. Bentley, C. Chandler, G. de Angelis, F. Della Vedova, A. Gadea, G. Hammond, S. M. Lenzi, N. Mărginean, D. R. Napoli, M. Nespolo, C. Rusu, and D. Tonev, Effective Charges in the fp Shell, Phys. Rev. Lett. **93**, 222501 (2004).

[47] M. Dufour and A. P. Zuker, Realistic collective nuclear Hamiltonian, Phys. Rev. C **54**, 1641 (1996).

[48] S. Schielke, K.-H. Speidel, O. Kenn, J. Leske, N. Gemein, M. Offer, Y. Y. Sharon, L. Zamick, J. Gerber, and P. Maier-Komor, First measurement and shell model interpretation of the g factor of the 2_1^+ state in self-conjugate radioactive ^{44}Ti, Phys. Lett. B **567**, 153 (2003).